

Reliable and Real-Time Highway Trajectory Planning via Hybrid Learning-Optimization Frameworks

Yujia Lu, Chong Wei, Lu Ma

Abstract—Autonomous highway driving presents a high collision risk due to fast-changing environments and limited reaction time, necessitating reliable and efficient trajectory planning. This paper proposes a hybrid trajectory planning framework that integrates the adaptability of learning-based methods with the formal safety guarantees of optimization-based approaches. The framework features a two-layer architecture: an upper layer employing a graph neural network (GNN) trained on real-world highway data to predict human-like longitudinal velocity profiles, and a lower layer utilizing path optimization formulated as a mixed-integer quadratic programming (MIQP) problem. The primary contribution is the lower-layer path optimization model, which introduces a linear approximation of discretized vehicle geometry to substantially reduce computational complexity, while enforcing strict spatiotemporal non-overlapping constraints to formally guarantee collision avoidance throughout the planning horizon. Experimental results demonstrate that the planner generates highly smooth, collision-free trajectories in complex real-world emergency scenarios, achieving success rates exceeding 97% with average planning times of 54 ms, thereby confirming real-time capability.

Index Terms—Autonomous driving, trajectory planning, mixed integer quadratic programming, graph neural networks, collision avoidance, highway driving.

I. INTRODUCTION

THE trajectory planning module plays a central role in ensuring driving safety in the modern autonomous driving system. It generates an optimal continuous trajectory for autonomous vehicles (AVs) over a future time horizon based on environmental information. This environmental information is provided by the perception module, which performs multi-sensor data fusion and feature extraction to produce real-time structured data through object detection and semantic segmentation. The control system then executes the planned trajectory by minimizing the deviation between the actual and intended vehicle behavior.

Highway scenarios are constrained within structured environments characterized by high-speed operation, low-curvature roadways, and standardized traffic regulations, typically involving only rule-compliant motorized vehicles. Key distinctions from urban environments [1] include: 1) longer anticipation horizons with a primary focus on forward roadway conditions; 2) simplified vehicle dynamics, featuring lower turning angles, no reverse maneuvers, and fewer braking

or acceleration events—yet with higher and more consistent speeds; and 3) increased collision risk due to high-speed operation. These characteristics heighten the importance of reliable collision avoidance in highway autonomous driving systems, while also necessitating low computational latency to respond to rapidly changing dynamic objects.

Collision avoidance reliability can be significantly improved through formally verified constraints that ensure safety properties under modeled assumptions. Rule-based methods offer deterministic implementation but rely on fixed logic, making them less effective in handling unforeseen complex scenarios. Optimization-based approaches provide greater adaptability by computing offline globally optimal or real-time feasible trajectories through objective-driven modeling with explicit physical and safety constraints. However, their computational efficiency is inherently constrained by the curse of dimensionality, especially when incorporating high-fidelity models or long-horizon predictions. Moreover, recursive suboptimality arising from approximate solutions or constraint relaxation may accumulate in iterative frameworks, ultimately degrading overall performance.

In optimization-based methods, planning problems that consider accurate collision avoidance are generally recognized as NP-hard, primarily because obstacles and vehicles are modeled as non-convex polygons [2]. Exact geometric computation techniques [2], [3] use symbolic representations and compute intersections, distances, and spatial arrangements through algorithms that guarantee mathematically exact results. These methods provide mathematical rigor and completeness but are computationally expensive and complex to implement. In highway motion planning, the environment is fast-changing and dynamic, rendering such computationally intensive collision constraints impractical. To address this, various approximations have been proposed. For example, the elliptical representation [4] simplifies computation but often introduces excessive conservatism, potentially causing deadlock maneuvers in narrow road scenarios. Alternatively, the multi-circle representation [5]–[7] offers improved fidelity, but it still results in non-convex collision regions.

Compared to rule-based and optimization-based approaches, learning-based methods demonstrate superior performance in high-dimensional state spaces and complex interaction scenarios. By employing deep neural networks to learn end-to-end mappings from environmental states to trajectories using large-scale, high-quality training data, these methods exhibit strong generalization capabilities within the training distribution. They are particularly effective in environments that lack tractable mathematical models or explicit rule-based representations. However, their reliance on data-driven approx-

Corresponding author: Chong Wei (e-mail: weichong@hainanu.edu.cn).

Yujia Lu is with the School of Traffic and Transportation, Beijing Jiaotong University, Beijing 100044, China (e-mail: 23311256@bjtu.edu.cn).

Chong Wei is with the School of Mechanical and Electrical Engineering, Hainan University, Hainan 570228, China.

Lu Ma is with the School of Traffic and Transportation, Beijing Jiaotong University, Beijing 100044, China (e-mail: lma@bjtu.edu.cn).

imation introduces inherent limitations, including a lack of interpretability and poor generalization to out-of-distribution scenarios. Due to the absence of explicit safety mechanisms, learning-based methods cannot inherently guarantee collision avoidance, especially in complex or rapidly changing environments.

Learning-based methods offer fast inference and capture complex behaviors, but may compromise safety. Optimization-based approaches ensure safety, yet often lack flexibility and impose a high computational burden. To combine their strengths, we propose a hybrid approach for trajectory planning in highway scenarios, with a strong emphasis on reliable collision avoidance and computational efficiency. The proposed framework adopts a two-layer structure. The upper layer employs a graph neural network (GNN) [8], trained on real-world highway data, to infer human-like velocity profiles by encoding multi-agent interactions as spatiotemporal graphs. The lower layer formulates path planning as a quadratic programming (QP) problem, enforcing hard constraints for collision avoidance and kinematic feasibility while optimizing for smoothness and traffic rule compliance. Although we adopt a GNN for the velocity prediction submodule, our hierarchical framework does not depend on any specific neural architecture. The contribution lies in the two-layer decomposition and the enforcement of hard constraints in the lower-layer optimizer. Other differentiable sequence-oriented architectures could be substituted with minimal change to the overall framework, provided they output a reasonable velocity profile.

In the proposed framework, our path optimization approach extends the work of Wang et al. [9], who modeled the problem as a mixed-integer quadratic programming (MIQP) formulation, employing a discretized geometric approximation of the ego vehicle (EV) body. This abstraction reflects the steering-induced variation in vehicle shape and can be interpreted as a variant of oriented bounding boxes (OBBs). While maintaining this geometric representation, our key contribution is a substantial reduction in binary variables by linearly approximating the nonlinearity of OBBs. This approximation preserves the success rate and yields notable improvements in computational efficiency. As another key contribution, the proposed method enforces hard collision-avoidance constraints on the final trajectory. Specifically, the geometric representation of the EV body imposes strict non-overlapping constraints with surrounding vehicles (SVs) in the spatial domain. Furthermore, by leveraging the upper-level velocity profile and the predicted trajectories of SVs, these spatial non-overlapping constraints are naturally extended into the temporal domain. This allows the enforcement of spatiotemporal constraints throughout the planning horizon, formally ensuring collision avoidance. Experiments demonstrate that our framework generates smooth trajectories with reliable collision avoidance across several safety-critical highway scenarios. When tested with a commercial solver, it achieves average runtimes of 54 ms for trajectory planning, proving real-time capability.

The remainder of this paper is organized as follows: Section II reviews the most related works. Section III presents the framework of the proposed hybrid trajectory planning method. Section IV details the trajectory discretization method

and vehicle kinematic model. Sections V and VI present the optimization-based path planning and learning-based velocity planning approaches, respectively. Section VII validates the method through experiments. Finally, Section VIII concludes the study.

II. RELATED WORK

A. Optimization-based Methods

A significant portion of optimization-based trajectory planning research decouples path and velocity planning, or separately addresses lateral and longitudinal motions. These components can be executed either sequentially or simultaneously. In sequential planning, a velocity profile is typically generated along a precomputed path [9], [10], or conversely, a path is planned based on a predefined velocity profile [11], [12]. In contrast, simultaneous planning considers spatial and temporal aspects jointly to improve trajectory optimality, but often relies on iterative optimization to refine trajectories under dynamic and safety constraints [13]–[16].

For lateral motion, a common approach [10], [15], [17] generates multiple coarse candidate paths using parametric curves, followed by evaluation and selection. Alternatively, other methods [9], [13], [18], [19] explicitly define collision-free feasible regions and perform trajectory optimization within these spatial constraints.

In trajectory optimization, some requirements must be strictly enforced as hard constraints to ensure system stability and reliability, while others can be incorporated as soft constraints to preserve adaptability and flexibility. Safety and kinematic/dynamic feasibility are typically modeled as hard constraints. Traffic rule compliance may also require hard constraints—such as speed limits and restrictions on reverse driving—while aspects like lane centering or minimizing successive lane changes are often treated as soft constraints. Similarly, objectives related to travel efficiency, energy consumption, and traffic flow harmony are generally modeled as soft constraints.

Studies that provide formal guarantees for safety and motion feasibility remain limited and are often based on rule-based approaches. For example, Chen et al. [20] pre-generate a curvature-continuous and kinematically feasible trajectory tree, then applied imitation learning to select the ego vehicle’s trajectory. Brudigam et al. [21] propose a triple-mode framework, with one mode specifically designed as a safety fallback to ensure trajectory integrity when needed. While safety is ideally modeled as a hard constraint, practical limitations—such as uncertainty, computational complexity, or incomplete information—often necessitate the use of soft constraints to approximate safety considerations. Many planners use probabilistic or predictive methods to avoid collisions. Representative implementations include game-theoretic frameworks [15], [22], artificial potential field (APF) methods [12], [23], [24], and predictive trajectory analysis of surrounding agents [22], [25], [26].

Among these practical limitations, computational complexity particularly stems from reformulating collision avoidance as hard constraints through mathematical optimization. One

major source of this complexity is the non-convex nature of explicit collision constraints in polygonal domains. To address this challenge, some studies [2], [3] have employed exact reformulations. These approaches are particularly targeted at spatially constrained scenarios, such as parking with limited maneuverability or navigating narrow roads. However, a series of works trade exactness for computational efficiency by adopting reasonable approximations, which inevitably introduce numerical errors that simplify implementation. Sun et al. [6] and Liu et al. [5] approximate non-convex collision avoidance constraints by iteratively constructing convex feasible sets around current trajectories, achieving high success rates. Han et al. [27] propose the RDA, solving a smooth biconvex reformulation that enables parallel computation of constraints per obstacle. Schäfer et al. [28] leverage reachability analysis to decompose non-convex free space into convex subsets and reformulate constraints via duality.

B. End-to-end Methods

While optimization-based methods focus on model-driven solutions, learning-based approaches are data-centric, requiring large-scale datasets or high-fidelity simulations. End-to-end frameworks have demonstrated the potential of deep learning in autonomous driving systems. For example, Nvidia [29] employs a convolutional neural network (CNN) to process camera inputs and directly predict steering angles, effectively unifying perception, planning, and control within a single model. Wayve [30] adopts reinforcement learning, using a monocular camera image, observed vehicle speed, and steering angle as inputs to generate steering commands and target speeds. Shanghai AI Lab [31] proposes a transformer-based pipeline that sequentially models perception, prediction, and planning, producing trajectories based solely on visual inputs.

However, due to the lack of formally defined constraints—particularly safety guarantees—end-to-end methods are generally not recommended for standalone deployment in real-world applications, although they can serve as components within broader systems. This limitation has led to a growing emphasis on hybrid architectures and hierarchical planning frameworks in recent research. Li et al. [32] propose a lane-changing framework that combines deep reinforcement learning (DRL) for high-level decision-making with quadratic programming for trajectory planning. To address highly complex and unstructured environments, especially in narrow areas, Li et al. [33] introduce a hierarchical planner in which a deep learning and Monte Carlo Tree Search (MCTS) module generates coarse paths, which are subsequently refined through optimization-based smoothing and velocity planning. Huang et al. [34] develop an end-to-end model to predict surrounding vehicle (SV) trajectories. These predictions are then fed into a differentiable nonlinear motion planner, enabling tight integration between prediction and planning.

While these approaches successfully integrate learning-based components into the planning pipeline, they typically rely on soft constraints or penalty-based formulations to handle safety requirements. In contrast, our approach not only leverages real-world datasets for prediction but also embeds

this supervised learning into a constraint-driven trajectory planner. This design explicitly accounts for the natural driving behavior and authentic traffic flow interactions in highway environments. It enables our planner to retain learning-based adaptability and reliably model decision-making in high-risk scenarios. Meanwhile, we enforce hard collision-avoidance constraints directly within the optimization layer, ensuring rule-compliant safety in the final output trajectory.

III. PROPOSED FRAMEWORK

Fig. 1 illustrates the proposed trajectory planning method, which adopts a decoupled motion framework consisting of two key modules: path planning and velocity planning. The velocity planning module employs an end-to-end neural network to predict longitudinal velocity profiles based on perception and prediction inputs. These profiles serve as dynamic constraints for the optimization-based path planner, which computes the lateral trajectory accordingly. The system processes upstream information—including EV/SV historical trajectories, road geometry, traffic rules, and SV predictions—to generate a coordinated motion plan in both longitudinal and lateral dimensions.

This study formulates path planning as a quadratic optimization problem, ensuring safety via hard collision-avoidance constraints, motion feasibility via kinematic and smoothness constraints, and compliance with traffic rules. The collision-avoidance constraints serve as the core of the proposed method, and their construction proceeds as follows. First, a heuristic search is employed to rapidly generate a safety corridor based on the velocity profile of the EV. This corridor defines the boundaries of the drivable space for the EV. Next, we construct rigorous spatiotemporal non-overlapping constraints with SVs by incorporating three key elements: the dynamic drivable space for the EV, the EV's longitudinal positions derived from the velocity planning layer, and a geometric representation of the EV body. To achieve a tighter fit to the actual shape of the vehicle, we design a discretized geometric representation of the EV body, which introduces nonlinear terms into the formulation. To further convexify the problem, we propose a linear approximation method that enables the formulation of a MIQP model, requiring only a small number of binary variables.

The velocity planning problem is formulated using a GNN, inspired by VectorNet [8]. While the framework itself is modular and agnostic to specific neural architectures, we adopt a GNN in this work due to its effectiveness in modeling structured multi-agent interactions. We construct a mapping from the observed system states to the future velocity profile of the EV via supervised learning, mimicking the speed decision-making behavior of human drivers. The velocity profile is represented as a sequence of longitudinal positions. Within this framework, the velocity planning module serves as the upper layer and provides reference inputs to the downstream path planning module. The final optimal trajectory of the EV is then generated by the path planner.

This framework provides two key benefits: safety enforcement and computational efficiency. The first refers to the enforcement of strict collision-avoidance constraints on the EV's

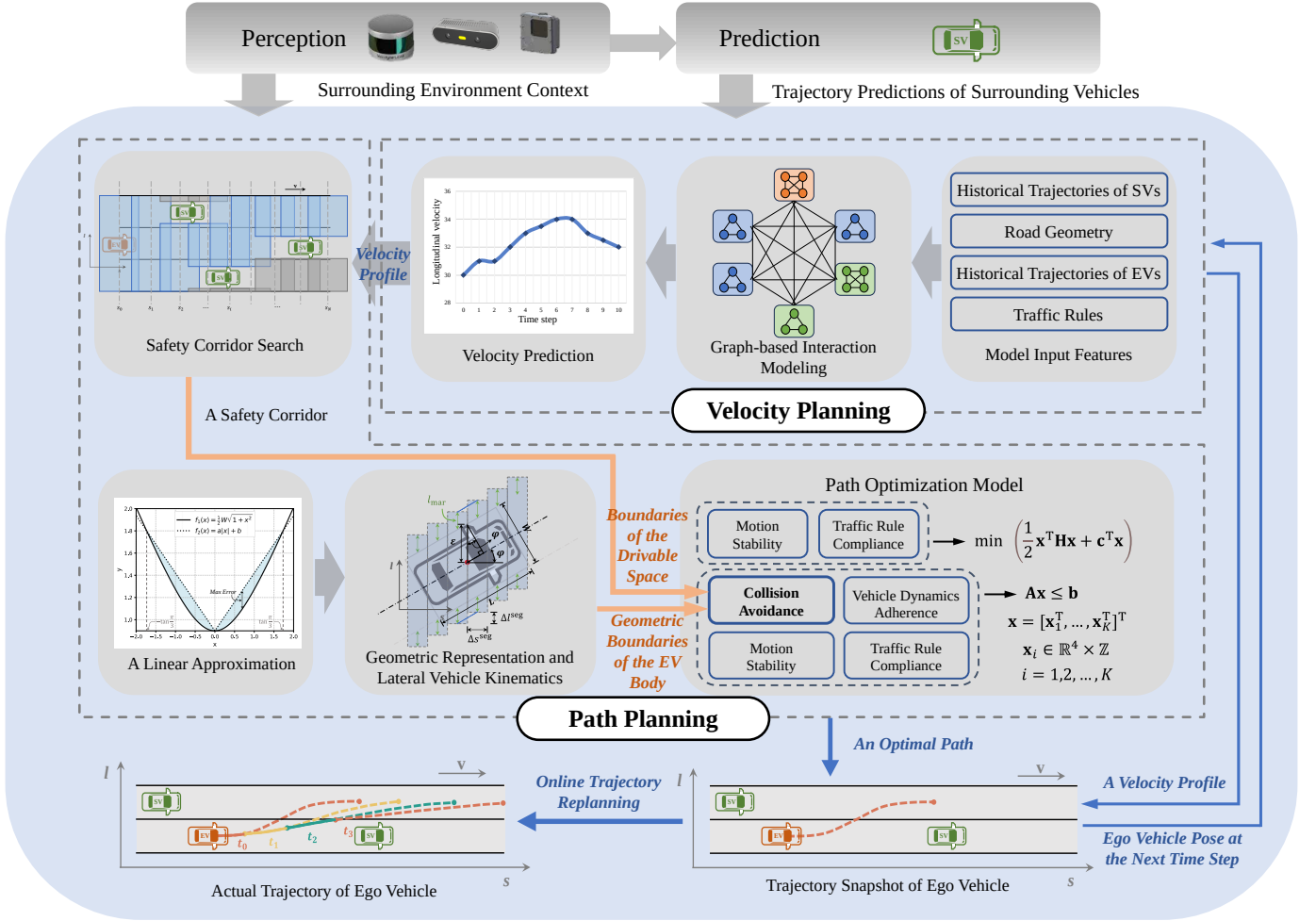


Fig. 1. Overall Framework of the Proposed Method

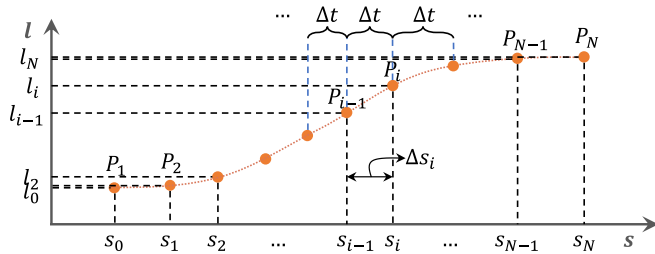


Fig. 2. Discretization of Vehicle Trajectory

trajectory, while the second results from improved convexity in the path optimization formulation and the lightweight design of the end-to-end velocity prediction model.

IV. TRAJECTORY GENERATION AND VEHICLE KINEMATIC MODEL

Typically, an s-l-t coordinate system is established to facilitate trajectory planning. In this system, the s-l coordinates define a Frenet frame [35], with the s-axis aligned with the road centerline and the l-axis orthogonal to it, while the t-axis corresponds to time. Discretizing the trajectory in this coordinate system is essential in autonomous driving, as it enables

efficient computation and facilitates constraint handling and control. Accordingly, the target trajectory is represented as a sequence of discrete points in the s-l-t space. As illustrated in Fig. 2, the trajectory is defined as a sequence of discrete points:

$$P = \{P_i\}_{i=1}^N, \quad P_i = (s_i, l_i, t_i), \quad i = 1, 2, \dots, N, \quad (1)$$

where N denotes the total number of discretization steps and a constant time interval

$$\Delta t = t_i - t_{i-1} \quad (2)$$

ensures uniform temporal resolution along the planning horizon.

This representation naturally decomposes the motion into longitudinal and lateral components, characterized by the sequences $\{s_i\}$ and $\{l_i\}$, respectively. Since Frenet coordinates can be transformed to and from the global Cartesian frame, the approach remains applicable to road segments with arbitrary curvature. The modeling and optimization of these discrete trajectories are detailed in Sections V and VI.

Although the planning framework operates on discrete trajectories, a continuous-time kinematic model is employed to describe the vehicle's motion and to enforce dynamic constraints. The vehicle state at time t is defined as a tuple

$(S(t), L(t), v(t), a(t), \varphi(t))$, where $(S(t), L(t))$ denotes the center-of-mass position of the vehicle in the Frenet frame; $v(t)$ and $a(t)$ represent the instantaneous velocity and acceleration, respectively; $j(t)$ is the jerk, defined as the time derivative of acceleration; and $\varphi(t)$ and $\omega(t)$ denote the heading angle (i.e., the angle between the velocity vector v and the reference s-axis) and the angular velocity. The system dynamics are given by:

$$\frac{d}{dt} \begin{bmatrix} S(t) \\ L(t) \\ v(t) \\ a(t) \\ \varphi(t) \end{bmatrix} = \begin{bmatrix} v(t) \cdot \cos \phi(t) \\ v(t) \cdot \sin \phi(t) \\ a(t) \\ j(t) \\ \omega(t) \end{bmatrix} \quad (3)$$

V. PATH PLANNING

A. Developing a Dynamic Path Optimization Model with MIQP

The path optimization problem considered in this study is formally defined as follows: Given the current kinematic states of the EV and SVs, the road geometry, and the EV's predefined longitudinal velocity profile, the objective is to compute an optimal dynamic path that 1) avoids any spatiotemporal occupancy conflict with SVs throughout the planning horizon, 2) satisfies the EV's kinematic constraints and relevant traffic rules, and 3) ensures smooth motion. We now present a detailed analysis demonstrating the effectiveness of the proposed modeling approach.

1) *Model Variable Definition*: By employing motion decoupling and discretization, the variables for this path optimization model are precisely defined. This approach transforms the path planning problem into an optimal solution search for variables \mathbf{x}_i , expressed as:

$$\mathbf{x}_i = (l_i, l'_i, l''_i, l'''_i), \quad \mathbf{x}_i \in \mathbb{R}^4, \quad i = 1, 2, \dots, N \quad (4)$$

In this context, l represents the EV's lateral position, measured at its geometric center. l' , l'' , and l''' denote its first-, second-, and third-order derivatives with respect to s , respectively. The relationship between l' and the heading angle φ is given by $l' = dl/ds = \tan \varphi$. The associated vehicle lateral kinematic model is presented in (19).

2) *Collision Avoidance Formulation*: Collision avoidance is primarily enforced through the following constraint set:

$$\begin{cases} l_i^{ub} + l_{\text{margin}} \leq ub_i \\ l_i^{lb} - l_{\text{margin}} \geq lb_i \end{cases} \quad (5)$$

Here, ub_i and lb_i represent the upper and lower boundaries of the drivable space for the EV at the i -th timestep, while l_i^{ub} and l_i^{lb} denote the upper and lower geometric boundaries of the EV body, respectively. l_{mar} represents the minimum safety margin between the EV and SVs. To efficiently determine these dynamic drivable regions, we propose a heuristic safety corridor search method in Section V-B. This method derives the final number of optimal trajectory sampling points, K , according to the safety corridor length.

However, when establishing the relationship between l_i^{ub}/l_i^{lb} and the model variable l_i , nonlinearity arises due to the unknown steering angle of the EV. To address this issue, a

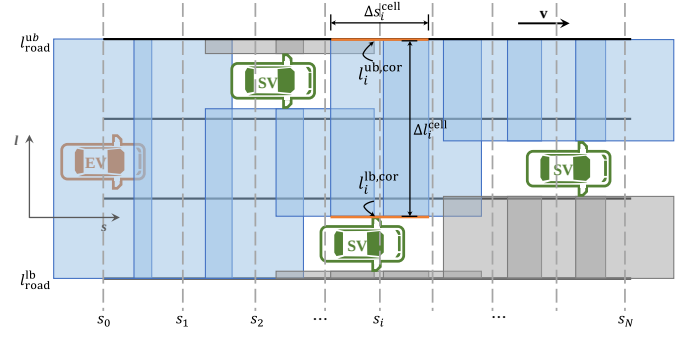


Fig. 3. Illustration of Safety Corridor Search

linear approximation method was developed to minimize the number of integer variables involved. Wang et al. [9] adopted a big-M formulation that introduced $Q \times N$ binary variables, where Q denotes the number of segments used to piecewise-linearize the nonlinear function. Compared with their method, our approach reduces the number of binary variables to N , denoted by k_i . Furthermore, to capture the shape of the vehicle body, a discretization technique was introduced, where the body is represented as a combination of small rectangles. This helps mitigate the conservatism introduced by approximating the vehicle with a single primitive rectangle. These two methods are detailed in Section V-C.

Consequently, based on (4), the path planning problem is reformulated as an optimization problem over the following variables \mathbf{x}_i :

$$\mathbf{x}_i = (l_i, l'_i, l''_i, l'''_i, k_i), \quad \mathbf{x}_i \in \mathbb{R}^4 \times \mathbb{Z}, \quad i = 1, 2, \dots, K \quad (6)$$

3) *Full problem formulation*: Beyond ensuring collision avoidance between the EV and SVs, the proposed model further incorporates additional objectives, including lateral kinematic consistency, motion smoothness, and adherence to highway traffic rules. As shown by (7), these considerations are jointly formulated as constraints and cost terms within a unified MIQP framework. For clarity, the detailed mathematical definitions of all constraints and objectives are presented in Section V-D.

$$\begin{aligned} \min \quad & \frac{1}{2} \mathbf{x}^\top \mathbf{H} \mathbf{x} + \mathbf{c}^\top \mathbf{x} \\ \text{s.t.} \quad & \mathbf{A} \mathbf{x} \leq \mathbf{b} \\ & \mathbf{x} = [\mathbf{x}_1^\top, \dots, \mathbf{x}_K^\top]^\top, \\ & \mathbf{x}_i = (l_i, l'_i, l''_i, l'''_i, k_i) \in \mathbb{R}^4 \times \mathbb{Z}, \quad i = 1, 2, \dots, K \end{aligned} \quad (7)$$

B. Safety Corridor Search Algorithm

The safety corridor is composed of discrete cells that represent optimal dynamic drivable regions for EV navigation. To efficiently identify these regions in real time, we employ a heuristic safety corridor search algorithm. This algorithm leverages available information, including the EV's current pose (position and orientation), its planned longitudinal motion, the current poses and predicted trajectories of SVs, road boundaries and lane markings. The search domain extends

along the s -axis of the Frenet frame and terminates at the final predicted longitudinal position of the EV. Fig. 3 illustrates an example of the safety corridor search, where the blue area denotes the optimal corridor and the gray areas indicate regions that were discarded. The heuristic algorithm works as follows:

Step 1: Generation of Longitudinal Reference Positions

A sequence of future longitudinal positions for the EV, denoted as $\mathcal{S} = \{s_1, s_2, \dots, s_N\}$, is used as the center positions of the safety cells distributed along the reference s -axis. The corresponding longitudinal lengths of these cells, $\{\Delta s_1^{\text{cell}}, \Delta s_2^{\text{cell}}, \dots, \Delta s_N^{\text{cell}}\}$, are computed in parallel using (14).

Step 2: Obstacle-Free Cell Identification

At each time step i corresponding to s_i , a scan-line sweeps laterally along the l -axis from $l_{\text{road}}^{\text{lb}}$ to $l_{\text{road}}^{\text{ub}}$, which are road boundaries. Obstacles intersecting the scan-line divide it into multiple segments. Each obstacle-free segment is stored as a rectangular cell $c_{i,d} \in \Sigma_i$, where $\Sigma_i = \{c_{i,1}, c_{i,2}, \dots, c_{i,D_i}\}$ denotes the set of candidate cells at step i . The length of each cell $c_{i,d}$ is Δs_i^{cell} , and the width of each cell $c_{i,d}$ is $\Delta l_{i,d}^{\text{cell}} = l_{i,d}^{\text{ub,cell}} - l_{i,d}^{\text{lb,cell}}$.

Step 3: Feasible Cell Selection

The candidate set Σ_i is filtered to obtain a feasible subset $\tilde{\Sigma}_i \subseteq \Sigma_i$, containing only cells that are wide enough to accommodate the EV. A cell $c_{i,d} \in \Sigma_i$ is retained if $\Delta l_{i,d}^{\text{cell}} \geq W_{\text{EV}} + 2l_{\text{buf}}$. W_{EV} and l_{buf} represent the ego EV's width and the lateral buffer distance required on each side of the vehicle, respectively. If $\tilde{\Sigma}_i$ is empty, the process proceeds directly to Step 5.

Step 4: Optimal Cell Selection

If $\tilde{\Sigma}_i$ contains only one cell, it is selected by default. Otherwise, the optimal cell is selected from $\tilde{\Sigma}_i$ as the one with the highest Intersection-over-Union (IoU) score relative to the selected cell from step $i-1$, based on spatial proximity. The optimal cell $c_{i,\text{optimal}}$ spans laterally over $[l_{i,\text{optimal}}^{\text{lb,cell}}, l_{i,\text{optimal}}^{\text{ub,cell}}]$.

Step 5: Termination Condition

If $i < N$, the process proceeds to Step 2 for time step $i+1$. Otherwise, the search terminates. The final output is a safety corridor defined by a sequence of lateral boundaries along the l -axis: $L^{\text{lb}} = \{l_1^{\text{lb,cor}}, l_2^{\text{lb,cor}}, \dots, l_K^{\text{lb,cor}}\}$ and $L^{\text{ub}} = \{l_1^{\text{ub,cor}}, l_2^{\text{ub,cor}}, \dots, l_K^{\text{ub,cor}}\}$, where each boundary satisfies $l_i^{\text{lb,cor}} = l_{i,\text{optimal}}^{\text{lb,cell}}$ and $l_i^{\text{ub,cor}} = l_{i,\text{optimal}}^{\text{ub,cell}}$. $K \leq N$ is the number of valid time steps with non-empty corridors.

C. Vehicle Geometric Representation and Linearization

1) *Linear Approximation:* Fig. 4 illustrates the relationship between the EV's body lateral boundaries ($l_i^{\text{ub}}, l_i^{\text{lb}}$) in (5) and its lateral position l_i :

$$\begin{cases} l_i^{\text{ub}} = l_i + \varepsilon_i \\ l_i^{\text{lb}} = l_i - \varepsilon_i \end{cases}, \quad i = 1, 2, \dots, K \quad (8)$$

where ε represents the lateral offset from the vehicle's geometric center to its boundary. The nonlinear dependence of ε

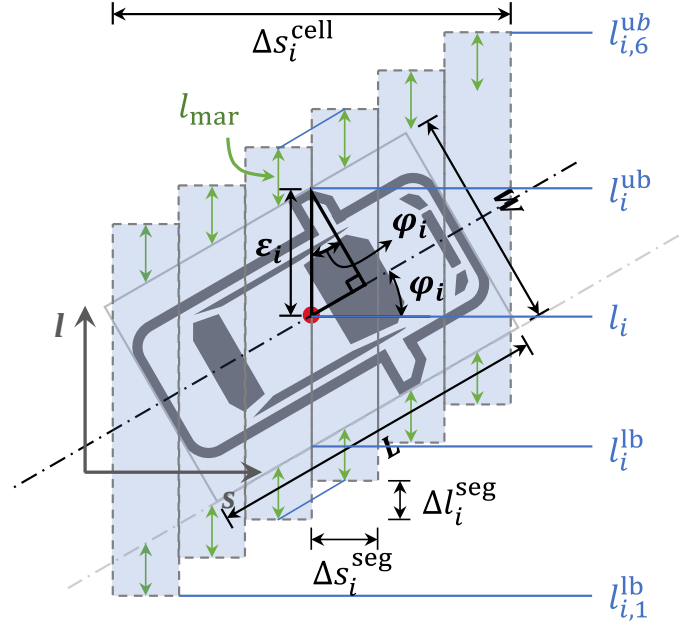


Fig. 4. Geometric Representation and Lateral Vehicle Kinematics

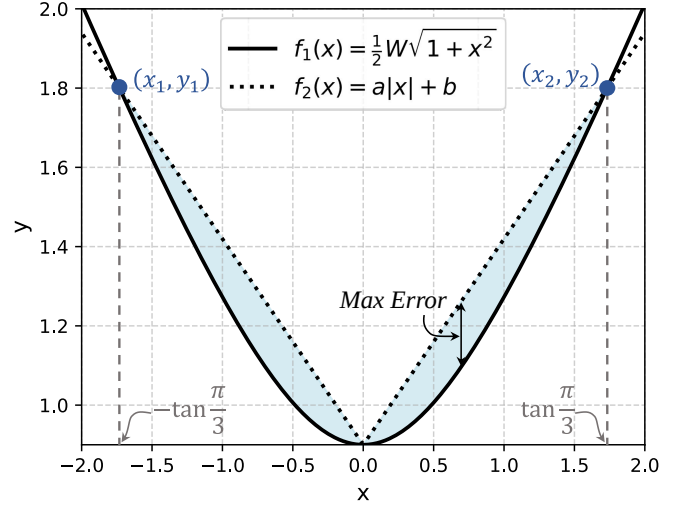


Fig. 5. A Linear Approximation to $f_1(x)$

on the heading angle φ arises from the fundamental kinematic relationship

$$\tan \varphi = \frac{dl}{ds} = l' \Rightarrow \varepsilon = f_1(l') = \frac{1}{2} W_{\text{EV}} \sqrt{1 + (l')^2}, \quad (9)$$

where W_{EV} denotes the EV's width. This nonlinear formulation would render the path-planning optimization model nonlinear, significantly compromising computational efficiency.

A linear approximation method is developed by leveraging the typically small steering angles in highway driving. Specifically, the maximum absolute EV heading angle is constrained to $|\varphi| \leq \pi/3$, which yields $\tan \varphi \in [-\tan(\pi/3), \tan(\pi/3)]$. Fig. 5 illustrates the piecewise-linear approximation of the absolute-value function constructed through endpoint fitting

at (x_1, y_1) , (x_2, y_2) , and the origin $(0, 0)$, where

$$\varepsilon = f_2(l') = a|l'| + b. \quad (10)$$

For a standard vehicle width $W_{EV} = 1.8$ m, the derived parameters yield $a \approx 0.5196$ and $b \approx 0.9$, producing a maximum approximation error of 0.1652 m within the operational domain (blue region, Fig. 5). Crucially, the inequality $f_2(l') \geq f_1(l')$ holds rigorously for all $l' \in [-\tan(\pi/3), \tan(\pi/3)]$, ensuring complete containment of the actual vehicle contour within the approximated geometry. This inherently preserves collision-avoidance guarantees while introducing only 16.5 cm of conservative margin in the worst-case scenario.

To implement the piecewise-linear approximation within the optimization framework, the formulation is convexified by introducing binary variables $k_i \in \{-1, 1\}$:

$$\varepsilon_i = a k_i l'_i + b, \quad (11)$$

with

$$k_i = \begin{cases} 1, & \text{if } l'_i \geq 0, \\ -1, & \text{if } l'_i < 0. \end{cases} \quad (12)$$

2) *EV's Geometric Representation*: Based on the linear approximation, we develop a discrete geometric representation that reduces computational complexity. As illustrated in Fig. 4, the vehicle body is discretized into $\lambda = 6$ rectangular segments oriented along the longitudinal s -axis. For each time step i , the length of each segment is determined by

$$\Delta s_i^{\text{seg}} = \frac{\Delta s_i^{\text{cell}}}{\lambda} \quad (13)$$

$$\Delta s_i^{\text{cell}} = \omega_{\text{cell}} v_i \quad (14)$$

where Δs_i^{cell} represents the longitudinal length of the i -th safety-corridor cell $c_{i,\text{optimal}}$, which fully encloses the vehicle body. This length scales proportionally with the EV's instantaneous velocity through the parameter ω_{cell} . The lateral offset between adjacent segments is calculated as

$$\Delta l_i^{\text{seg}} = \Delta s_i^{\text{seg}} \tan \varphi_i = \Delta s_i^{\text{seg}} l'_i. \quad (15)$$

This approach yields the following boundary constraints for the vehicle's geometric representation:

$$\begin{cases} l_{i,j}^{\text{ub}} = l_i^{\text{ub}} + (j - \frac{\lambda+1}{2}) \Delta s_i^{\text{seg}} l'_i & i = 1, 2, \dots, K; \\ l_{i,j}^{\text{lb}} = l_i^{\text{lb}} + (j - \frac{\lambda+1}{2}) \Delta s_i^{\text{seg}} l'_i & j = 1, 2, \dots, \lambda. \end{cases} \quad (16)$$

D. Constraints and Objective Function

1) Collision Avoidance Constraints

$$\begin{cases} l_{i,j}^{\text{ub}} + l_{\text{mar}} \leq l_i^{\text{ub},\text{cor}} & i = 1, 2, \dots, K; \\ l_{i,j}^{\text{lb}} - l_{\text{mar}} \geq l_i^{\text{lb},\text{cor}} & j = 1, 2, \dots, \lambda. \end{cases} \quad (17)$$

Derived from (5) and (16), and the safety-corridor boundaries, these constraints incorporate the discretized upper and lower boundaries $(l_{i,j}^{\text{ub}}, l_{i,j}^{\text{lb}})$ of the EV geometry. The parameter K represents the number of trajectory samples covered by the safety-corridor search (Section V-B).

2) Road Boundary Constraints

The EV must remain within the road boundaries during highway driving. The road boundaries, defined by the lower boundary $l_{\text{road}}^{\text{lb}}$ and upper boundary $l_{\text{road}}^{\text{ub}}$, are obtained through perception modules or HD maps. This constraint is formally expressed as

$$l_{\text{road}}^{\text{lb}} \leq l_i \leq l_{\text{road}}^{\text{ub}}. \quad (18)$$

3) Vehicle Lateral Kinematic Constraints

The enhanced lateral kinematic model extends the conventional point-mass formulation by incorporating vehicle geometric shape, establishing the equality constraints in (19). The derivation employs a third-order Taylor expansion about s_{i-1} applied to the interval $\Delta s_i = s_i - s_{i-1}$. Given initial conditions (l_0, l'_0, l''_0) , motion continuity between planning cycles is ensured. The kinematic constraints are formulated as

$$\begin{cases} l''_i = l''_{i-1} + l'''_i \Delta s_i \\ l'_i = l'_{i-1} + l'_i \Delta s_i + \frac{1}{2} l''_i (\Delta s_i)^2 \\ l_i = l_{i-1} + l'_i \Delta s_i + \frac{1}{2} l''_i (\Delta s_i)^2 + \frac{1}{6} l'''_i (\Delta s_i)^3 \end{cases} \quad (19)$$

and the vehicle's physical limits impose constraints on state derivatives

$$\begin{cases} l'_{\min} \leq l'_i \leq l'_{\max} \\ l''_{\min} \leq l''_i \leq l''_{\max} \\ l'''_{\min} \leq l'''_i \leq l'''_{\max} \end{cases}. \quad (20)$$

4) Objective Function

$$\begin{aligned} \min \omega_1 \sum_{i=1}^N (l_i - l_{\text{ref},i})^2 &+ \omega_2 \sum_{i=1}^N (l'_i)^2 + \omega_3 \sum_{i=1}^N (l''_i)^2 \\ &+ \omega_4 \sum_{i=1}^N (l'''_i)^2 + \omega_5 \sum_{i=2}^N (l_i - l_{i-1})^2 + \omega_6 \sum_{i=2}^N (l'_i - l'_{i-1})^2 \end{aligned} \quad (21)$$

The weighting coefficients ω_1 – ω_6 balance competing objectives. ω_1 addresses lane centering by minimizing deviation from the reference waypoints $l_{\text{ref},i}$ to maintain optimal lane positioning. ω_2 – ω_4 promote trajectory smoothness by penalizing the first, second, and third derivatives of lateral displacement, ensuring smooth path geometry, while ω_5 and ω_6 minimize jumps in lateral position and slope between adjacent waypoints, reducing discretization-induced irregularities.

The reference waypoints $l_{\text{ref},i}$ are determined online based on available lane information. For cells with lane markings, $l_{\text{ref},i}$ follows the appropriate lane centerline. In multi-lane scenarios, the algorithm selects the lane that minimizes deviation from the previous reference trajectory. For unmarked regions, $l_{\text{ref},i}$ defaults to the cell center.

VI. VELOCITY PLANNING

We adopt and modify the VectorNet [8] framework to map historical states to the future longitudinal motion of EVs. While retaining VectorNet's hierarchical graph structure and vectorized encoding of HD maps and vehicle kinematics, our model reformulates the prediction from 2D position sequences to longitudinal motion, enabling more direct modeling of EV longitudinal behavior. This design allows the model to learn from real-world trajectories how drivers regulate velocity and spacing in response to SVs, capturing realistic car-following

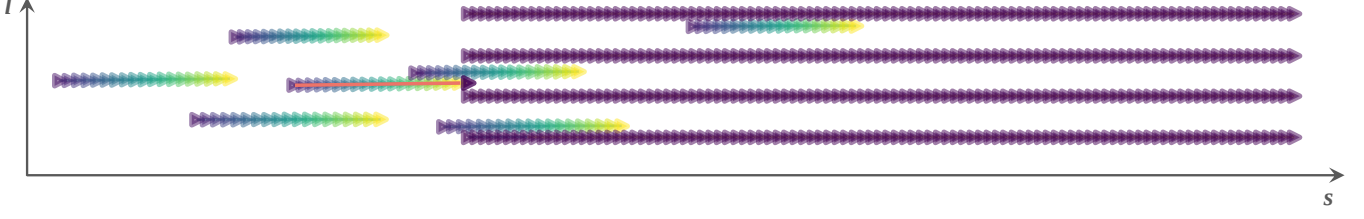


Fig. 6. Vectorized Representation of Trajectories and Map Features

dynamics and complex traffic flow adaptations. By doing so, it reflects human-like decision-making patterns observed in authentic highway scenarios. Leveraging both local and global interactions, the proposed framework achieves state-of-the-art accuracy in behavior prediction under high-speed driving conditions.

A. End-to-End Velocity Prediction Framework

To prepare data for velocity prediction, we apply a temporal sliding-window sampling strategy and standardize trajectory data into fixed-length sequence. This approach enhances training robustness by increasing trajectory diversity and generating a richer set of agent motion samples.

Based on this preprocessing strategy, we extract features including kinematic states of the EV and SV, as well as static map features. These features are organized as uniformly sampled time-series sequences over a fixed observation window and transformed into vectorized representations (see Section VI-B).

To capture the interactions among traffic entities, the network architecture builds on the hierarchical graph framework described in [8]. Vectorized features form nodes within subgraphs, where each subgraph corresponds to a short-duration local observation of a traffic entity—such as an EV, SV, or map element—and is modeled as a polyline. These subgraphs interact through attention mechanisms, creating a global interaction graph that captures complex traffic relationships. The output layer then produces discretized velocity predictions (see Section VI-C).

The parameters of the model are updated by using mini-batch stochastic gradient descent (SGD), minimizing the mean squared error between predicted and ground-truth velocity sequences across all timesteps. By learning from human driving data, the model captures realistic velocity control patterns. The loss function is defined as:

$$L = \frac{1}{N} \sum_{i=1}^N (y_i - \hat{y}_i)^2 \quad (22)$$

B. Trajectory and Map Feature Encoding

The highway environment comprises both dynamic traffic participants and static map elements (e.g., lane markings), which are encoded using distinct feature representation schemes. Trajectory features capture spatiotemporal characteristics such as positions, velocities, accelerations, while map features include geometric coordinates and semantic labels.

The vectorization process transforms continuous trajectories and map annotations into graph-compatible representations, as defined in (23), where each vector vec_i corresponds to a graph node, enriched with the following feature descriptors:

$$\begin{cases} \text{vec}_i = \{d_i^s, d_i^e, \text{id}_i^{\text{time}}, \text{id}_i^{\text{object}}, \text{id}_i^{\text{local}}, \text{id}_i^{\text{global}}\} \\ d_i = \{s_i, l_i, \text{vel}_i^s, \text{vel}_i^l, \text{acc}_i^s, \text{acc}_i^l\} \end{cases} \quad (23)$$

where

- $i = 1, 2, \dots, M - 1$.
- d_i^s and d_i^e represent the kinematic states at the start and end points of vec_i , respectively. Each state comprises the position coordinates (s_i, l_i) , velocities $(\text{vel}_i^s, \text{vel}_i^l)$, and accelerations $(\text{acc}_i^s, \text{acc}_i^l)$, where the superscripts s and l denote the longitudinal and lateral directions, respectively.
- $\text{id}_i^{\text{time}}$ denotes the timestamp associated with the vector.
- $\text{id}_i^{\text{object}}$ specifies the object type, where 1 indicates EV, 2 indicates SV, and 3 indicates the lane marking in this paper.
- $\text{id}_i^{\text{local}}$ denotes the polyline subgraph index that vec_i belongs to. Each traffic entity is represented by a unique polyline, and this index groups vectors accordingly.
- $\text{id}_i^{\text{global}}$ denotes the index of the observation timestamp associated with the vector. This index is unique across the entire dataset and encodes the global temporal position of each vector.

For map features, all dynamic state variables—namely $\text{id}_i^{\text{time}}$, vel_i^s , vel_i^l , acc_i^s and acc_i^l —are set to zero, as they are not applicable to static elements. For trajectory data, the parameter $M = M_{\text{tra}}$ defines the length of the historical observation window, representing the number of time steps backward from the current time of the EV. For map data, $M = M_{\text{map}}$ specifies the number of sampled points along the road ahead of the EV's current position. Given a spatial sampling interval of d_s , the total forward view distance for map features is computed as $M_{\text{map}} \times d_s$ meters.

Fig. 6 illustrates the vectorized encoding scheme using a purple-to-yellow color gradient to indicate temporal progression, with the EV's trajectory highlighted in red. Each arrowed segment represents a vectorized node, and consecutive nodes form polyline subgraphs, shown as connected segments. The temporal resolution is uniform across the representation: both the intra-vector duration (from the start to end point of a vector) and the inter-vector interval are fixed at Δt .

C. Velocity Profile Representation

The graph neural network outputs a discretized velocity profile for the EV, represented as a sequence of longitudinal velocities $\mathbf{V} = (v_1, v_2, \dots, v_N)$ over N future time steps, where N is determined by the discretization scheme defined in Section IV. Given a fixed temporal interval Δt , the corresponding longitudinal positions $\mathbf{S} = (s_1, s_2, \dots, s_N)$ can be obtained via the kinematic relation

$$s_i = \sum_{j=0}^i v_j \Delta t, \quad i = 1, 2, \dots, N. \quad (24)$$

This representation enforces compliance with traffic rules by applying a sigmoid activation at the output layer, scaled to the range $(0, v_{\max})$ based on the road's speed limit. By construction, the velocity cap serves as a safety mechanism that prevents extreme outputs (e.g., overspeeding), without negatively impacting accuracy when applied to representative, real-world data.

VII. EXPERIMENTS

The proposed framework was implemented in Python, integrating Gurobi v11 [36] for path optimization and PyTorch for velocity prediction. All experiments were conducted on a computational platform equipped with an Intel i9-9900 CPU (3.60 GHz), 32GB of RAM, and an NVIDIA RTX 2080 Ti GPU, running Ubuntu 18.04. Real-world human driving trajectories were sourced from the HighD dataset [37], with all test scenarios drawn from a held-out subset that was entirely separate from the training data used for model development.

Section VII-A evaluates the trajectory planner in three challenging highway scenarios involving mixed autonomy, where the EV operates autonomously alongside human-driven SVs. Section VII-B quantitatively analyzes the system's computational efficiency and solution robustness. Section VII-C details the training procedure and empirical performance of the learning-based velocity predictor. The complete parameter configurations are provided in Table I.

The experiment adopts a receding-horizon planning strategy, as illustrated in Fig. 1, where the optimal trajectory is re-optimized every dt to reflect the current state. The temporal framework is governed by three key parameters: a unified sampling rate of 0.1 s, used both as the trajectory discretization interval (Δt) and the replanning cycle (dt); a 3-second planning horizon; and a 2-second observation horizon. These settings correspond to 30 planning steps ($N = 3 \text{ second}/0.1 \text{ second}$) and 20 observation steps ($M_{\text{tra}} = 2 \text{ second}/0.1 \text{ second}$) for algorithmic implementation.

A. Validation on Real-World Emergency Scenarios

The HighD dataset involves vehicles traveling at high speeds (25–40 m/s), characteristic of typical highway driving environments. We analyze three representative scenarios in which the EV faces safety challenges. In all cases, the proposed method successfully generates trajectories that enable the EV to perform emergency evasive maneuvers while maintaining high smoothness and kinematic feasibility. These results validate the method's effectiveness in safety-critical situations

TABLE I
PARAMETER CONFIGURATIONS

Parameters	Values
$dt, \Delta t, N, M_{\text{tra}}, M_{\text{map}}$	0.1 s, 0.1 s, 30, 20, 100
$\lambda, l_{\text{mar}}, l_{\text{buf}}, \omega_{\text{cell}}$	6, 0.3 m, 0.5 m, 0.5
$\omega_1, \omega_2, \omega_3, \omega_4, \omega_5, \omega_6$	1, 500, 500, 500, 500, 500
$l'_{\min}, l''_{\min}, l'''_{\min}$	$-\tan(\pi/3), -3, -3$
$l'_{\max}, l''_{\max}, l'''_{\max}$	$\tan(\pi/3), 3, 3$
W_{EV}, L_{EV}	1.8 m, 4.8 m
Input and Output Feature Dimensions	15, 1
Learning Rate, Decaying Factor, Batch Size	0.001, 0.9, 128
Loss Function, Optimizer	MSE, Adam
Train-Validation-Test Split	7:2:1
v_{\max}	50 m/s

and demonstrate its robustness under extreme conditions. This also suggests its reliability in less complex, lower-risk environments.

1) Scenario 1: Cut-In by a Slower Frontal Vehicle

This scenario involves a typical emergency cut-in event, where a slower target vehicle (TV) abruptly merges into the EV's lane. Fig. 7 shows the scenario performance with sequential snapshots, kinematic metrics, and lane-change trajectories. The EV is consistently shown in orange-red across all visualizations, while the SVs are depicted using the same set of colors across subsequent figures to ensure clarity.

The TV—shown in blue and located in the left-front position—begins indicating a lane-change intention at $t = 3$ s and crosses into the EV's lane at $t = 4.5$ s, initiating a collision risk due to the 7 m/s velocity differential. Emergency braking at the EV's current speed of 32 m/s would not only result in high longitudinal jerk and compromised ride comfort, but also significantly increase the risk of rear-end collisions. This risk stems from the combination of short headway and high speed, particularly given the limited reaction time available to drivers of following human-driven vehicles. To mitigate these risks, the proposed planner initiates an early evasive lane change at $t = 3$ s, leveraging 0.1-second replanning cycles to generate dynamically optimized trajectory segments (blue dashed). These segments collectively form a highly smooth, collision-free executed trajectory (orange) that safely avoids the TV within 5 s while preserving passenger comfort—as reflected by the kinematic profile with peak acceleration $\leq 0.8 \text{ m/s}^2$ and maximum heading angle of 5° . This demonstrates the planner's ability to maintain trajectory quality and ride comfort under frequent online updates, even in critical collision scenarios.

2) Scenario 2: Cut-In by a Close-Decelerating Frontal Vehicle

Scenario 2 resembles Scenario 1 but presents a more urgent situation. It involves a slower-moving TV (shown in purple in Fig. 8a) that is initially positioned in the left-front of the EV and much closer in proximity. At $t = 3$ s, the TV suddenly initiates a hazardous lane change toward the EV's lane. As it approaches the lane boundary, it becomes nearly parallel to the EV, creating an imminent risk of a sideswipe collision if the EV fails to respond. Meanwhile, emergency

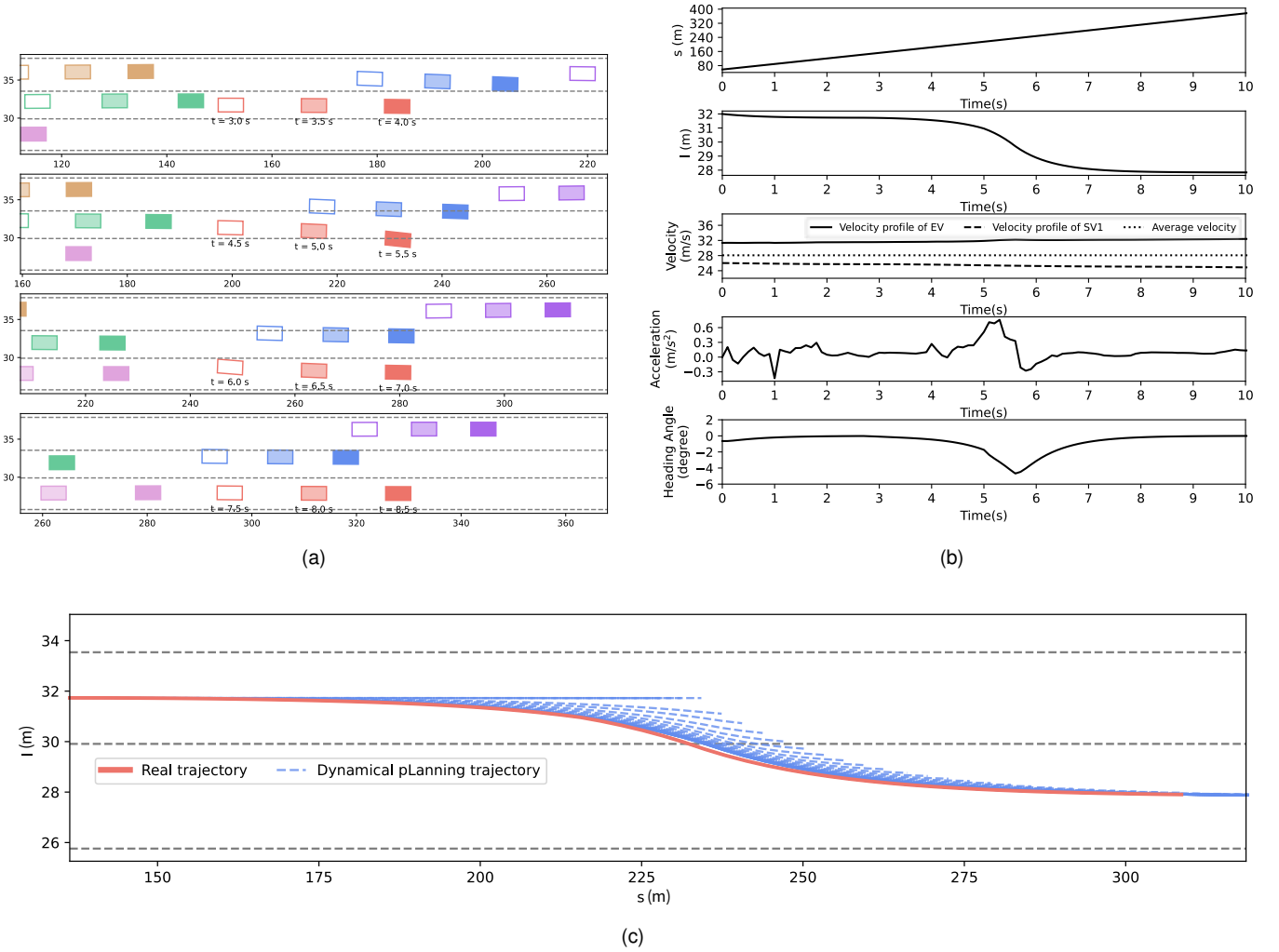


Fig. 7. Scenario 1 Performance. (a) Sequential snapshots at 0.5-second intervals; (b) kinematic profile showing longitudinal and lateral displacement, velocity, acceleration, and heading angle. In the velocity plot, SV1 corresponds to the blue vehicle shown in (a); (c) the full executed lane-change trajectory along with intermediate trajectory snapshots from online re-planning.

braking would also introduce a significant risk of rear-end collision. To mitigate both risks, the proposed planner triggers a defensive lane change to the right at $t = 4$ s, guiding the EV into an adjacent lane while maintaining a nearly constant velocity (≈ 32 m/s). The maneuver is completed by $t = 7.5$ s with sustained safe lateral clearance from the intruding TV. The smooth kinematic response—characterized by a peak acceleration below 0.5 m/s² and a maximum heading angle of 5° , as shown in Fig. 8b and Fig. 8c—demonstrates the system’s capability for stable and comfortable lateral control in time-critical interactions.

3) Scenario 3: Cut-In by a High-Speed Rear Vehicle

Scenario 3 addresses a dynamic cut-in event involving a TV (shown in green in Fig. 9a) approaching from the EV’s right-rear at 33 m/s. At $t = 6$ s, the TV suddenly initiates a lane change into the EV’s lane, creating an immediate sideswipe-collision risk. In response, the planner promptly initiates an evasive left-lane change into an adjacent lane with sufficient forward clearance, completing the avoidance maneuver within 4 s. As shown in Figs. 9b–9c, the EV maintains smooth and

TABLE II
SUCCESS RATES ACROSS RECORDINGS

Recording Index	Scenarios	Scenario Success Rate (%)	Cycle Success Rate (%)
53	2421	96.1	98.1
54	2313	97.5	98.7
55	2166	97.3	98.8

stable motion throughout, with all kinematic metrics remaining within safe operational limits. This result further confirms the planner’s robustness in handling fast-developing, high-risk scenarios via real-time trajectory adaptation.

B. Computational Efficiency and Success Rate

The proposed method was validated through 591,213 trajectory planning trials across 6,900 driving scenarios extracted from recordings 53 to 55 of the HighD dataset. As shown in Fig. 10, the planning cycle runtime refers to the total time required to generate a complete trajectory per planning cycle,

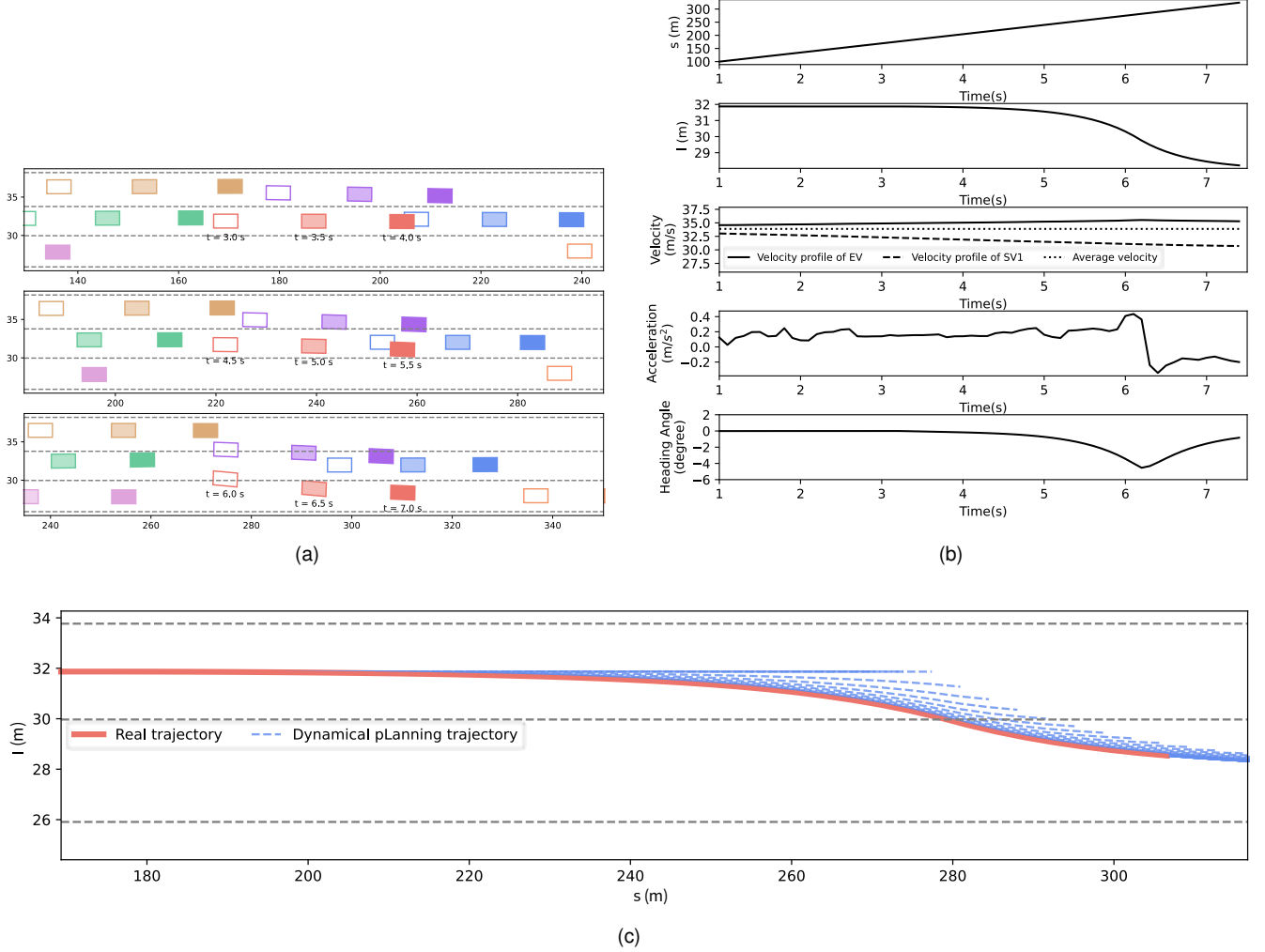


Fig. 8. Scenario 2 Performance. (a) Sequential snapshots at 0.5-second intervals; (b) kinematic profile showing longitudinal and lateral displacement, velocity, acceleration, and heading angle. In the velocity plot, SV1 corresponds to the purple vehicle shown in (a); (c) the full executed lane-change trajectory along with intermediate trajectory snapshots from online re-planning.

encompassing velocity prediction, path optimization, and state updates. It primarily falls within the range of 45–65 ms (mean: 54.2 ms; median: 52.6 ms). As shown in Fig. 11, within this cycle, the MIQP-based path optimization accounts for 7–15 ms (mean: 11.2 ms; median: 10.7 ms). These results highlight the computational efficiency of both the proposed hybrid framework and its underlying models.

Two success criteria were used to evaluate the robustness of the planner. The first is the scenario success rate, which measures the ability to generate feasible trajectories throughout the ground-truth time horizon. The second is the cycle success rate, which reflects the feasibility of single-step planning. As presented in Table II, the method achieves a 97.0% scenario success rate across all locations. Compared to MIQP-TP [9], our method replaces the handcrafted velocity planner with an end-to-end model, which improves the flexibility of feasible trajectory generation. In contrast, the approximation of nonlinear collision-avoidance constraints is made more conservative by increasing the safety margins, which typically increases the difficulty of obtaining feasible solutions. Despite these

TABLE III
DISPLACEMENT ERRORS IN MOTION PREDICTION

	Baseline	Velocity Planning (Ours)
Epochs	25	100
Prediction Target	Trajectory	Velocity profile
ADE (m)	1.66	0.63
FDE (m)	3.67	1.46

tighter constraints, our method achieves a 4.5 percentage point improvement in scenario success rate (from 92.5% to 97.0%) over method [9], while maintaining a high cycle success rate. This demonstrates the reliable performance of the proposed planning framework in structured, high-speed traffic scenarios.

C. Training and Evaluation of the Velocity Prediction Model

The neural network architecture was trained using the hyperparameters listed in Table I. Trajectory data were extracted from three-lane HighD scenarios (recordings 26–45) and split into training (317,588 samples), validation (90,739 samples),

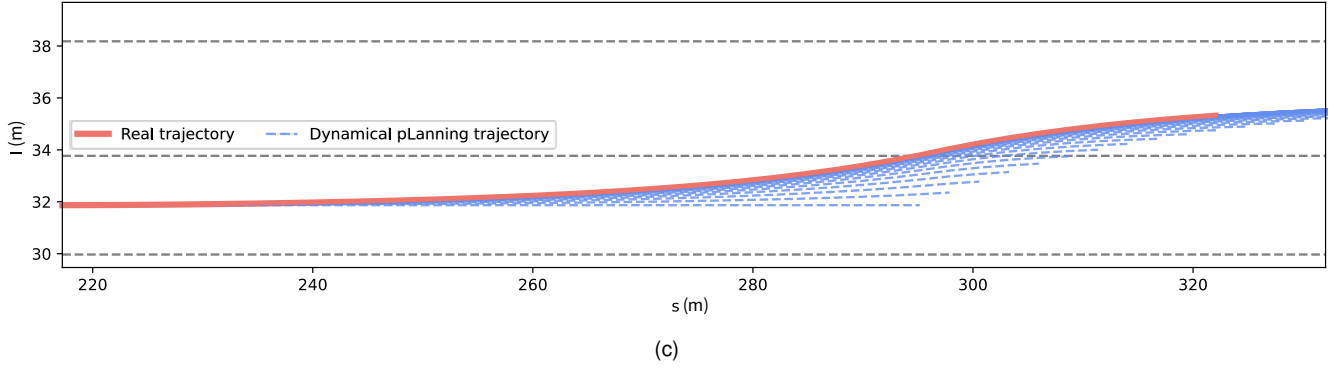
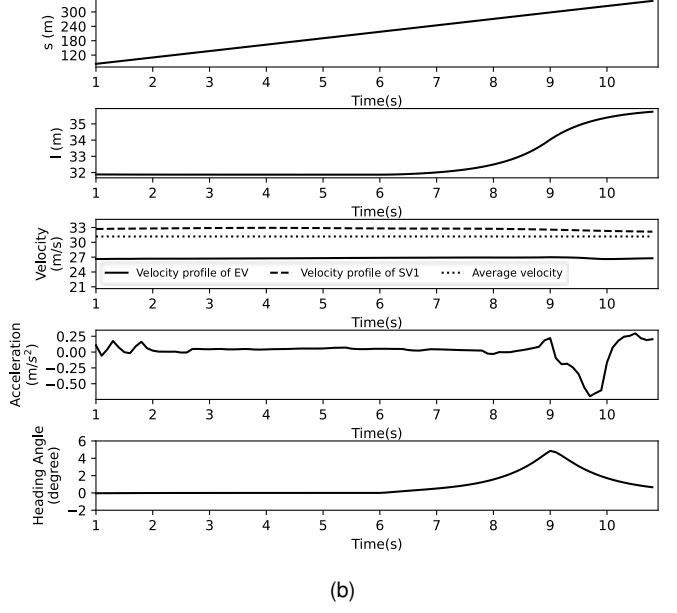
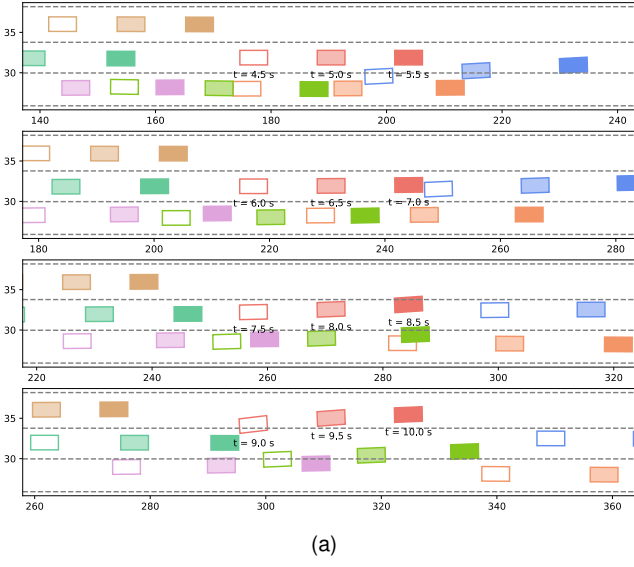


Fig. 9. Scenario 3 Performance. (a) Sequential snapshots at 0.5-second intervals; (b) kinematic profile showing longitudinal and lateral displacement, velocity, acceleration, and heading angle. In the velocity plot, SV1 corresponds to the green vehicle shown in (a); (c) the full executed lane-change trajectory along with intermediate trajectory snapshots from online re-planning.

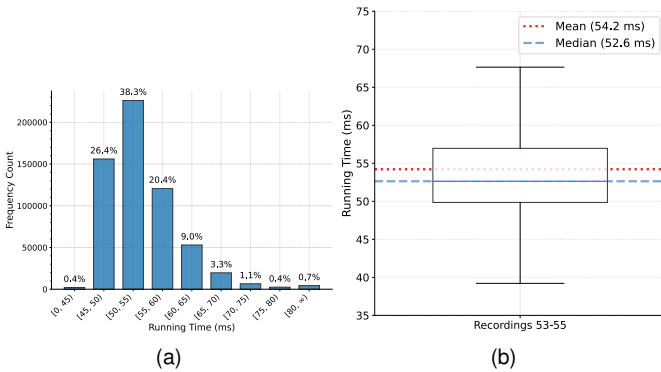


Fig. 10. Distribution of Planning Cycle Runtimes. For clarity, values below 45 ms and above 80 ms are grouped at the axis limits, and box plot outliers are omitted.

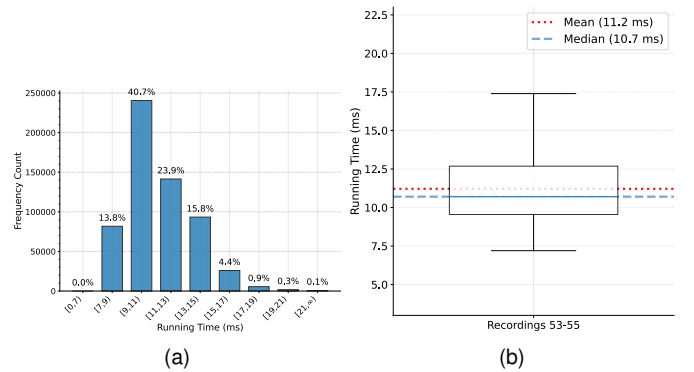


Fig. 11. Distribution of Path Optimization Time. For clarity, values above 21 ms are capped at axis limits, and box plot outliers are omitted.

and test (45,371 samples) sets in a 7:2:1 ratio. As shown in Fig. 12, the training process exhibited stable convergence, achieving a mean test loss of 0.84 m/s after 100 epochs.

Comparative evaluation against the baseline method [8] demonstrates that our approach achieves lower displacement error (DE) in velocity prediction (Table III). As our model

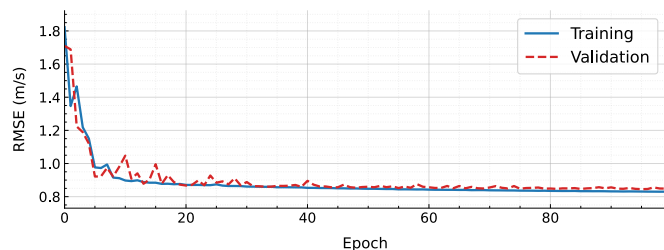


Fig. 12. Velocity Prediction Error Over Iterations

outputs discrete velocity sequences, we apply (24) to transform these predictions into positional coordinates, thereby enabling DE computation. This metric serves as both an intuitive and widely adopted measure for assessing motion prediction accuracy. The evaluation uses recordings 53-55, which comprise 121,934 trajectories sampled with a 1-second sliding window. This improvement stems from our model's specialized focus on longitudinal motion, whereas the baseline jointly predicts both longitudinal and lateral trajectories. This finding implies that a notable portion of displacement error arises from limited lateral motion prediction accuracy. By explicitly focusing on longitudinal kinematics, the proposed method avoids this source of error and better leverages the strengths of the VectorNet backbone, which is particularly well-suited for structured trajectory representations in the longitudinal domain.

The model began to stabilize after approximately 20 epochs. This trend was consistent with the baseline method, which exhibited similar convergence behavior around 25 epochs. To address kinematic irregularities observed during preliminary validation, training was extended to 100 epochs. The additional iterations improved motion smoothness without compromising prediction accuracy, producing smoother acceleration profiles that are critical for ride comfort.

VIII. CONCLUSIONS

This paper presents a hybrid trajectory planning framework for autonomous highway driving that integrates optimization-based and learning-based approaches, featuring an upper-layer velocity planner and a lower-layer path planner, with collision avoidance as the primary focus. A GNN-based model predicts a human-like longitudinal velocity profile, serving as the dynamic basis for path optimization. A heuristic safe corridor and discretized vehicle geometry representation enable the formulation of spatiotemporal non-overlapping constraints, ensuring collision-free trajectories. Experiments in three real-world emergency scenarios validate the method's reliable collision avoidance, while preserving trajectory smoothness and kinematic feasibility. We employ a linear approximation for the EV's geometry to enable MIQP formulation, enhancing computational efficiency. Real-world highway experiments demonstrate strong performance: average path planning takes 11.2 ms with 54.2 ms planning cycles, achieving over 97% success rates in high-speed structured scenarios. Our framework effectively balances safety, reliability, and computational efficiency for autonomous driving applications.

REFERENCES

- [1] L. Claussmann, M. Revilloud, and D. Gruyer, "A review of motion planning for highway autonomous driving," *IEEE Transactions on Intelligent Transportation Systems*, vol. 21, no. 5, pp. 1826–1848, 2020.
- [2] J. Fan, N. Murgovski, and J. Liang, "Exact obstacle avoidance for autonomous vehicles in polygonal domains," *IEEE Transactions on Systems, Man, and Cybernetics: Systems*, vol. 54, no. 10, pp. 5964–5976, 2024.
- [3] X. Zhang, A. Liniger, and F. Borrelli, "Optimization-based collision avoidance," *IEEE Transactions on Control Systems Technology*, vol. 29, no. 3, pp. 972–983, 2021.
- [4] J. Fan, N. Murgovski, and J. Liang, "Efficient optimization-based trajectory planning for unmanned systems in confined environments," *IEEE Transactions on Intelligent Transportation Systems*, vol. 25, no. 11, pp. 18 547–18 560, 2024.
- [5] T. Liu, R. Chai, and S. Chai, "Fast collision-free multi-vehicle lane change motion planning and control framework in uncertain environments," *IEEE Transactions on Industrial Electronics*, vol. 71, no. 12, pp. 16 602–16 613, 2024.
- [6] C. Sun, Q. Li, and B. Li, "A successive linearization in feasible set algorithm for vehicle motion planning in unstructured and low-speed scenarios," *IEEE Transactions on Intelligent Transportation Systems*, vol. 23, no. 4, pp. 3724–3736, 2022.
- [7] C. Wei, Y. Wang, and Y. Asakura, "A nonlinear programming model for collision-free lane-change trajectory planning based on vehicle-to-vehicle communication," *Journal of Transportation Safety & Security*, vol. 13, no. 9, pp. 936–956, 2019.
- [8] J. Gao, C. Sun, H. Zhao, Y. Shen, D. Anguelov, C. Li, and C. Schmid, "Vectornet: Encoding hd maps and agent dynamics from vectorized representation," in *Proceedings of the IEEE/CVF Conference on Computer Vision and Pattern Recognition (CVPR)*, June 2020.
- [9] Y. Wang, C. Wei, and S. Li, "A convex trajectory planning method for autonomous vehicles considering kinematic feasibility and bi-state obstacles avoidance effectiveness," *IEEE Transactions on Vehicular Technology*, vol. 73, no. 7, pp. 9575–9590, Jul. 2024.
- [10] W. Lim, S. Lee, and M. Sunwoo, "Hybrid trajectory planning for autonomous driving in on-road dynamic scenarios," *IEEE Transactions on Intelligent Transportation Systems*, vol. 22, no. 1, pp. 341–355, 2021.
- [11] Z. Zhang, L. Zhang, and J. Deng, "An enabling trajectory planning scheme for lane change collision avoidance on highways," *IEEE Transactions on Intelligent Vehicles*, vol. 8, no. 1, pp. 147–158, 2023.
- [12] Y. Yan, J. Wang, and Y. Wang, "A cooperative trajectory planning system based on the passengers' individual preferences of aggressiveness," *IEEE Transactions on Vehicular Technology*, vol. 72, no. 1, pp. 395–406, 2023.
- [13] L. Xiong, Y. Zhang, and Y. Liu, "Integrated decision making and planning based on feasible region construction for autonomous vehicles considering prediction uncertainty," *IEEE Transactions on Intelligent Vehicles*, vol. 8, no. 11, pp. 4515–4523, 2023.
- [14] X. Lin, T. Wang, and S. Zeng, "Autonomous vehicles lane-changing trajectory planning based on hierarchical decoupling," *IEEE Transactions on Intelligent Transportation Systems*, vol. 25, no. 12, pp. 20 741–20 752, 2024.
- [15] Z. Zhang, C. Wang, and W. Zhao, "Path-speed decoupling planning method based on risk cooperative game for intelligent vehicles," *IEEE Transactions on Transportation Electrification*, vol. 10, no. 2, pp. 3792–3806, Jun. 2024.
- [16] Y. Liu, B. Zhou, and X. Wang, "Dynamic lane-changing trajectory planning for autonomous vehicles based on discrete global trajectory," *IEEE Transactions on Intelligent Transportation Systems*, vol. 23, no. 7, pp. 8513–8527, 2022.
- [17] F. Tarhini, R. Talj, and M. Doumiani, "Safe and energy-efficient jerk-controlled speed profiling for on-road autonomous vehicles," *IEEE Transactions on Intelligent Vehicles*, pp. 1–16, 2024.
- [18] E. I. Liu and M. Althoff, "Specification-compliant driving corridors for motion planning of automated vehicles," *IEEE Transactions on Intelligent Vehicles*, vol. 8, no. 9, pp. 4180–4197, 2023.
- [19] S. Manzingier, C. Pek, and M. Althoff, "Using reachable sets for trajectory planning of automated vehicles," *IEEE Transactions on Intelligent Vehicles*, vol. 6, no. 2, pp. 232–248, 2021.
- [20] X. Chen, S. Cheng, and S. Li, "Lateral and longitudinal integrated emergency collision avoidance system with handling stability guarantee," *IEEE Transactions on Transportation Electrification*, vol. 10, no. 3, pp. 4930–4940, 2024.
- [21] T. Brudigam, M. Olbrich, and D. Wollherr, "Stochastic model predictive control with a safety guarantee for automated driving," *IEEE Transactions on Intelligent Vehicles*, vol. 8, no. 1, pp. 22–36, 2023.

- [22] Y. Chen, S. Li, and X. Tang, "Interaction-aware decision-making for autonomous vehicles," *IEEE Transactions on Transportation Electrification*, vol. 9, no. 3, pp. 4704–4715, 2023.
- [23] P. Rousseas, C. Bechlioulis, and K. Kyriakopoulos, "Trajectory planning in unknown 2d workspaces: A smooth, reactive, harmonics-based approach," *IEEE Robotics and Automation Letters*, vol. 7, no. 2, pp. 1992–1999, 2022.
- [24] Y. Huang, H. Ding, and Y. Zhang, "A motion planning and tracking framework for autonomous vehicles based on artificial potential field elaborated resistance network approach," *IEEE Transactions on Industrial Electronics*, vol. 67, no. 2, pp. 1376–1386, 2020.
- [25] L. Cheng, Y. Qin, and K. Yang, "Toward safe motion planning for autonomous driving in highway," *IEEE Transactions on Vehicular Technology*, vol. 74, no. 2, pp. 2491–2502, Feb. 2025.
- [26] J. Zhou, B. Olofsson, and E. Frisk, "Interaction-aware motion planning for autonomous vehicles with multi-modal obstacle uncertainty predictions," *IEEE Transactions on Intelligent Vehicles*, vol. 9, no. 1, pp. 1305–1319, Jan. 2024.
- [27] R. Han, S. Wang, and S. Wang, "Rda: An accelerated collision free motion planner for autonomous navigation in cluttered environments," *IEEE Robotics and Automation Letters*, vol. 8, no. 3, pp. 1715–1722, 2023.
- [28] L. Schafer, S. Manzinger, and M. Althoff, "Computation of solution spaces for optimization-based trajectory planning," *IEEE Transactions on Intelligent Vehicles*, vol. 8, no. 1, pp. 216–231, 2023.
- [29] M. Bojarski, D. Del Testa, D. Dworakowski, B. Firner, B. Flepp, P. Goyal, L. D. Jackel, M. Monfort, U. Muller, J. Zhang, X. Zhang, J. Zhao, and K. Zieba, "End to End Learning for Self-Driving Cars," p. arXiv:1604.07316, Apr. 2016.
- [30] A. Kendall, J. Hawke, D. Janz, P. Mazur, D. Reda, J.-M. Allen, V.-D. Lam, A. Bewley, and A. Shah, "Learning to drive in a day," in *2019 International Conference on Robotics and Automation (ICRA)*, 2019, pp. 8248–8254.
- [31] Y. Hu, J. Yang, L. Chen, K. Li, C. Sima, X. Zhu, S. Chai, S. Du, T. Lin, W. Wang, L. Lu, X. Jia, Q. Liu, J. Dai, Y. Qiao, and H. Li, "Planning-oriented autonomous driving," in *Proceedings of the IEEE/CVF Conference on Computer Vision and Pattern Recognition*, 2023.
- [32] S. Li, C. Wei, and Y. Wang, "Combining decision making and trajectory planning for lane changing using deep reinforcement learning," *IEEE Transactions on Intelligent Transportation Systems*, vol. 23, no. 9, pp. 16 110–16 136, 2022.
- [33] H. Li, P. Chen, and G. Yu, "Trajectory planning for autonomous driving in unstructured scenarios based on deep learning and quadratic optimization," *IEEE Transactions on Vehicular Technology*, vol. 73, no. 4, pp. 4886–4903, 2024.
- [34] Z. Huang, H. Liu, and J. Wu, "Differentiable integrated motion prediction and planning with learnable cost function for autonomous driving," *IEEE Transactions on Neural Networks and Learning Systems*, vol. 35, no. 11, pp. 15 222–15 236, Nov. 2024.
- [35] M. Werling, J. Ziegler, and S. Kammel, "Optimal trajectory generation for dynamic street scenarios in a frenét frame," in *2010 IEEE Intelligent Vehicles Symposium*, 2010, pp. 987–993.
- [36] G. Optimization, *Gurobi Optimizer Reference Manual*, 2024.
- [37] R. Krajewski, J. Bock, L. Kloeker, and L. Eckstein, "The highd dataset: A drone dataset of naturalistic vehicle trajectories on german highways for validation of highly automated driving systems," in *2018 21st IEEE International Conference on Intelligent Transportation Systems (ITSC)*, Maui, Hawaii, USA, 2018, pp. 2118–2125.